PERGAMON

Journal of Asian Earth Sciences 21 (2002) 175–188

Journal of Asian Earth Sciences

www.elsevier.com/locate/jseaes

Crystallization and melting experiments of a fluorine-rich leucogranite from the Xianghualing Pluton, South China, at 150 MPa and H_2O-saturated conditions

Xiao-Lin Xiong[a,b,*], Bing Rao[b], Fan-Rong Chen[a], Jin-Chu Zhu[b], Zhen-Hua Zhao[a]

[a]*Guangzhou Institute of Geochemistry, Chinese Academy of Sciences, Guangzhou 510640, People's Republic of China*
[b]*State Key Laboratory of Mineral Deposit Research, Nanjing University, Nanjing 210093, People's Republic of China*

Received 3 September 2001; revised 13 March 2002; accepted 29 March 2002

Abstract

Crystallization and melting experiments were conducted with a fluorine-rich granite from the Xianghualing Pluton, South China, in order to determine its crystallization sequence and melt fractionation trends at 150 MPa and H_2O-saturated conditions, which are close to the crystallization conditions of this pluton. The experimental results showed that quartz is the liquidus phase and is sequentially followed by K-rich alkali feldspar, zinnwaldite, albite, and topaz. There are obvious evolutionary trends in the compositions of alkali feldspar and residual melt with decreasing temperature from liquidus to 600 °C. The Or ($KAlSi_3O_8$) content in alkali feldspar increases and the contents of Ab ($NaAlSi_3O_8$) and An ($CaAl_2Si_2O_8$) decrease. The most apparent fractionation trends in residual melt compositions are decreases in the SiO_2 and K_2O contents and Si/Al ratio, and increases in the contents of Na_2O, F, Al_2O_3, CaO, and the ratios of A/NKC and Na/K. These experimental results indicate that a low-silica and sodic granitic melt could be derived from a relatively high-silica and potassic F-rich leucogranitic magma via fractional crystallization. They also shed light on the fractional crystallization and vertical zoning of the Xianghualing Pluton and other similar high-level, F-rich leucogranite plutons.

Keywords: Xianghualing Pluton; Vertical zoning; F-rich granite; Crystallization and melting experiments

1. Introduction

Fluorine-rich leucogranitic rocks, such as topaz granites and their volcanic equivalents, topaz rhyolites, have low Ca, Fe, Mg, and Ti contents and are usually peraluminous. These special felsic rocks are highly differentiated and enriched in fluorine and incompatible lithophile elements including Li, Be, Rb, Cs, W, Sn, Nb, Ta, U, Th, etc. and may be associated with ore deposits of various combinations of these elements. Many F-rich plutons have a characteristic vertical zonation from a relatively potasssic and siliceous zone upward to a sodic and silica-poor zone towards the apex. The fluorine content of these granitic rocks is mostly in the range of 0.5–1.5 wt% (Bailey, 1977; Burt et al., 1982; Pichavant and Manning, 1984; Pollard, 1995). Some extreme differentiates, such as ongonites, topaz rhyolites and residual melts (trapped within melt inclusions), contain >2 wt% fluorine (Kovalenko, 1973; Congdon and Nash, 1988; Kortemeier and Burt, 1988; Webster and Duffield, 1991; Webster et al., 1996; Zhu et al., 1993, 2001; Raimbault and Burnol, 1998; Liu et al., 1999). The special petrogenesis and melt properties, and the economic significance of these rocks have greatly stimulated the experimental investigations of phase equilibria and physical and chemical properties in F-containing granitic systems. Experimental investigations have demonstrated that fluorine strongly lowers the liquidus and solidus temperatures and enlarges the liquidus fields of quartz relative to the liquidus field of feldspar (Wyllie and Tuttle, 1961; Koster van Groos et al., 1968; Kovalenko, 1978; Manning, 1981; Webster et al., 1987; Weidner and Martin, 1987; London et al., 1989; Xiong et al., 1999). Fluorine also depolymerizes the granitic melt structure (Mysen and Virgo, 1985), and greatly reduces the viscosity and density of silicate melts (Dingwell et al., 1985, 1993) and increases the diffusion coefficients (Dingwell, 1985). These experimental results have contributed greatly to the understanding of the genesis of F-rich

* Corresponding author. Address: Guangzhou Institute of Geochemistry, Chinese Academy of Sciences, Guangzhou 510640, People's Republic of China. Tel.: +86-20-8529-0287; fax: +86-20-8529-0139.
E-mail address: xiongxl@gig.ac.cn (X.L. Xiong).

1367-9120/02/$ - see front matter © 2002 Elsevier Science Ltd. All rights reserved.
PII: S1367-9120(02)00030-5

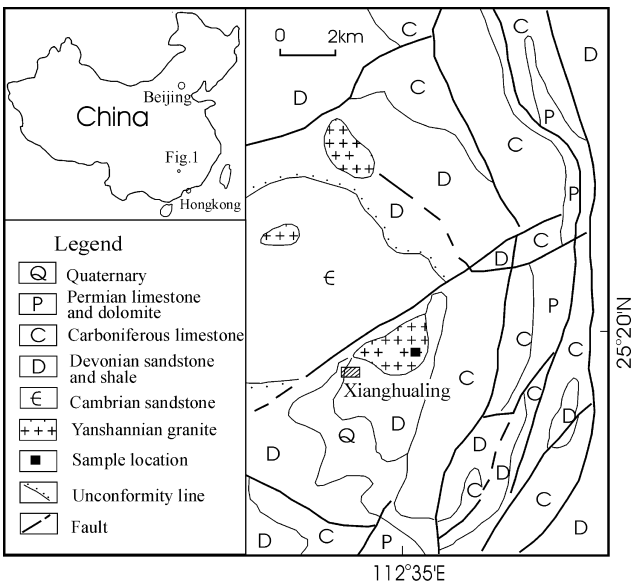

Fig. 1. Geological map of the Xianghualing area (after Huang and Du (1988)) showing the major lithologic units and sample location.

granitic rocks and the transport properties, mobility, and eruption behavior of such magmas.

In this paper, we selected a natural example of fluorine-rich granite from Xianghualing Pluton, South China, to determine experimentally its solidus and liquidus temperatures, crystallization sequence and melt fractionation trends at 150 MPa and H_2O-saturated conditions. These experimental conditions (see below) are approximately equivalent to those for the crystallization of this pluton, and accordingly the experimental results can be related to the chemical fractionation and zoning of the Xianghualing Pluton and the other similar F-rich plutons.

2. Xianghualing Pluton and Petrography of the experimental sample

The Xianghualing Pluton is located near the center of the EW-trending Nanling Range of South China. It is about 20 km north of Linwu town, Southern Hunan Province. The pluton was emplaced approximately 155 m.y. ago (Huang and Du, 1988) at a shallow level in the crust, intruding Paleozoic limestone, dolomite, and arenaceous and argillaceous rocks (Fig. 1). The thickness of these Paleozoic strata is about 5 km (Huang and Du, 1988), indicating that the lithostatic pressure is approximately 150 MPa at the top of the pluton.

The Xianghualing Pluton has an outcrop of 2.2 km^2 on the surface and is characterized by a well-developed vertical zonation (Hu and Sun, 1984; Huang and Du, 1988; also see Fig. 4B). From the top downward, the following four zones in the apical region of the pluton are identified:

1. Pegmatoid stockscheider zone (0.5–3 m thick), consisting of the heterogeneously distributed pegmatitic minerals quartz, K-feldspar, topaz, and zinnwaldite.
2. Greisen zone (30–70 m thick), lying directly under the pegmatoid stockscheider zone. It is predominantly medium grained (3–5 mm) and equigranular except that the uppermost part (2–5 m thick) is horizontally banded, coarse grained and, in places, pegmatitic. The major constituents are quartz (30–65 vol%), zinnwaldite (15–35%), and topaz (15–30%). Accessory minerals in order of relative abundance include fluorite, cassiterite, wolframite, tantalite, columbite, sulfides and Hf-rich zircon.
3. Albite granite zone (about 60 to over 100 m thick). It is usually fine to medium grained (0.5–5 mm). The major minerals are albite (35–55%), quartz (25–35%), microcline (10–25%), zinnwaldite and lepidolite (3–10%), and topaz (3–7%). Accessory minerals in relative abundance-order are fluorite, microlite, tantalite, Hf-rich zircon, cassiterite, wolframite, and sulfides.
4. Albite–microcline granite zone, which is the dominant part of the pluton. It is usually medium grained (1–5 mm) and consists of quartz (30–35%), microcline (30–35%), albite (25–30%), zinnwaldite (2–8%), and topaz (2–4%). Accessory minerals are mainly zircon, apatite, fluorite, rutile, sulfides. The W–Sn, and Nb–Ta minerals are rare in this zone.

The greisen and pegmatoid stockscheider, which are closely associated with W and Sn mineralization, may have formed by metasomatism during postmagmatic hydrothermal alteration (Hu and Sun, 1984), whereas the albite granite and albite–microcline granite are believed to have formed dominantly by magmatic processes (Zhu et al., 1993; Chang and Huang, 1998). There are many melt inclusions containing aqueous fluid in quartz and topaz (Chang and Huang, 1998) and miarolitic cavities in these rocks (Huang and Du, 1988; Chang and Huang, 1998), indicating that the parent magma was rich in H_2O and was saturated with H_2O prior to complete crystallization. The transition between albite–microcline granite and albite granite is typically gradational in mineralogy and major element chemistry. From the lower level upwards, the SiO_2 and K_2O contents decrease, and the contents of Al_2O_3, Na_2O and F increase, in agreement with the aforesaid variation of mineralogy between both zones (Hu and Sun, 1984; Huang and Du, 1988). Similarly, from albite–microcline granite to albite granite, there is a systematic increase in the contents of incompatible lithophile trace elements and ore metals, including Li, Rb, Cs, W, Sn, Nb, Ta. In places, Ta and Nb can be enriched to economic concentrations in the albite granite zone.

The sample was collected from the albite–microcline granite zone, which can approximately represent much of the parent magma of the pluton, owing to the much larger volume of albite–microcline granite relative to its upper variants. Quartz is anhedral in the sample. Microcline

Table 1
Compositions of the starting material and some hydrous quenched glasses (wt%)

	SG(w)[a]	SGG(w)[b]	SGG(m)[c]	C01(m)[d]	C02(m)[d]
SiO_2	75.31	75.18	75.25 ± 0.85	71.35 ± 0.96	70.93 ± 1.25
TiO_2	0.02	0.01	0.01 ± 0.01	<0.01	<0.01
Al_2O_3	13.76	13.75	13.78 ± 0.56	13.08 ± 0.37	13.05 ± 0.43
FeO[e]	1.63	1.60	1.62 ± 0.08	1.52 ± 0.07	1.49 ± 0.05
MnO	0.13	0.13	0.10 ± 0.06	0.08 ± 0.05	0.09 ± 0.03
MgO	0.09	0.08	0.08 ± 0.02	0.08 ± 0.03	0.07 ± 0.05
CaO	0.36	0.36	0.37 ± 0.10	0.34 ± 0.12	0.33 ± 0.11
Na_2O	3.83	3.86	3.67 ± 0.13	3.08 ± 0.32	3.05 ± 0.36
K_2O	4.78	4.75	4.61 ± 0.11	4.37 ± 0.17	4.35 ± 0.16
Li_2O	0.16	0.15	n.d.[f]	n.d.	n.d.
P_2O_5	0.05	0.04	0.03 ± 0.02	0.04 ± 0.05	0.02 ± 0.03
H_2O	0.20	–	n.d.	n.d.	n.d.
F	0.95	0.96	0.92 ± 0.15	0.91 ± 0.13	0.90 ± 0.18
2F=O	−0.38	−0.40	−0.39	−0.38	−0.38
Total	100.69	100.47	100.05	94.48	93.91
A/NKC[g]	1.14	1.13	1.18	1.25	1.27
Na/K[g]	1.25	1.22	1.20	1.09	1.07

[a] Starting granite, analyzed by wet chemical techniques.
[b] Starting granite glass, analyzed by wet chemical techniques.
[c] Starting granite glass, analyzed by electron microprobe.
[d] Hydrous quenched glasses at superliquidus temperatures (see Table 2: C01, 800 °C; C02, 780 °C) analyzed by electron microprobe; The results for electron microprobe analysis (c and d) are the average of 5 analyses for each sample. The 1-σ uncertainties are listed.
[e] Fe total as FeO.
[f] Not determined.
[g] A/NKC and Na/K, respectively, are the molar ratios of $Al_2O_3/Na_2O + K_2O + CaO$ and Na_2O/K_2O.

occurs as 'patch' microperthite and the K-rich host is turbid and appears untwinned. Albite appears as discrete euhedral grains. Zinnwaldite is interstitial and appears largely to be primary. Topaz occurs as clear, equant, anhedral grains and is generally included in zinnwaldite flakes. Equant and anhedral grains of purple fluorite were observed occasionally, and some accessory minerals, such as zircon and apatite, occur as inclusions in the zinnwaldite. Based on the inclusion/host and overgrowth relationships of the minerals, the crystallization of major phases began with quartz and microcline and was followed sequentially by albite, zinnwaldite, and topaz (and fluorite).

3. Experimental methods

3.1. Starting material preparation

Two starting materials were used for the experiments; one was the albite–microcline granite (powder) and another was its glass. The granite sample was crushed and ground into powder as large as 20–50 μm and was employed as the starting material of melting experiments. It was analyzed for major elements by wet-chemical methods (column 1 in Table 1). The composition is highly leucogranitic with high SiO_2 (75.31%), slightly peraluminous (A/NKC = 1.14), moderate Na_2O/K_2O (1.25), high F (0.95%) and low concentrations of cafemic constituents (CaO, FeO, MgO, MnO, and TiO_2).

The albite–microcline granite glass was used as another starting material in crystallization experiments and crystallization–melting experiments. The glass was prepared by melting the granite powder at 1400 °C in sealed platinum containers for approximately 4 h; two cycles of melting and grinding were performed to improve chemical homogeneity. The glass was then ground to <50 μm for use in experiments. The composition of the glass was analyzed by both wet chemical techniques and electron microprobe (columns 2 and 3 in Table 1), and is nearly identical to that of the original granite, except for the relatively low Na_2O content analyzed by microprobe (discussed below).

3.2. Experimental procedures

Each experimental charge consisted of about 50 mg of starting solid material and 10 wt% H_2O to maintain H_2O saturation. The choice of H_2O saturation agrees approximately with the H_2O-rich magma of the Xianghualing Pluton. Experimental charges were loaded and sealed into gold capsules (25 × 4.8 mm, thickness 0.2 mm) by electric-arc welding. These capsules were weighed before and after welding to check for leakage. Experiments were conducted in rapid-quench cold seal vessels at the Key State Laboratory of Mineral Deposit Research in Nanjing University. The vessels were pressurized with water and heated in solid tube furnaces with a horizontal orientation. The portion of the cold end of the pressure vessel outside of the furnace was cooled by a water circulating jacket during

the experiment. At the end of an experimental run the vessel was removed from the furnace and tilted vertically allowing the capsule to slide into the cool end of the vessel; the charge was quenched to room temperature in a matter of seconds. After quenching, the capsule was removed from the pressure vessel, then cleaned, dried, and weighed to check for leakage during the run.

The experimental pressure was 150 MPa, corresponding to about 5 km of emplacement depth of the Xianghualing Pluton. Pressure was monitored by Bourdon tube pressure gauges, which were periodically calibrated against factory-calibrated Heise gauges. Run temperatures were in the range of 500–800 °C and were measured by platinum–rhodium thermocouples calibrated against certified thermocouples and the melting point of NaCl at 1 atm. Pressure is believed to be accurate to ±3 MPa. Temperature is believed to have an uncertainty of ±3 °C including the error in the thermocouple calibration and the uncertainty due to the temperature gradient along the capsules. The fugacity of oxygen in the experiments was not explicitly controlled, but was buffered close to nickel–nickel oxide by the Ni-rich pressure vessel and the pressure medium (water). Runs lasted about 7–30 days for the crystallization experiments and the crystallization–melting experiments and 10–15 days for the melting experiments.

Crystallization experiments and crystallization–melting experiments were performed on both sides of equilibrium to determine the liquidus temperature and crystallization sequence (the order of the crystal appearance temperature). The crystallization experiments approached the liquidus and crystal appearance temperatures from the high-temperature side at decreasing temperature intervals of approximately 20 °C using crystal-free glasses as the starting material. The crystallization–melting experiments approached the liquidus and crystal appearance temperatures from the low-temperature side at increasing temperature intervals of 10 °C. These crystallization–melting experiments consisted of two-stage runs (similar to those of Pichavant (1987)). In the first stage (crystallization stage), the run temperature was one known from the crystallization experiments to produce partial crystallization. In the second stage (dissolution or melting stage), the run temperature was raised isobarically to the final temperature and kept steady. The second stage run therefore is a melting experiment of crystals formed in the first stage run to examine if crystal dissolution took place. Each of the liquidus and crystal-appearance temperatures was located between the temperature of either a crystallization experiment or a crystallization–melting experiment showing evidence of crystal growth and that of a crystallization–melting experiment showing evidence of crystal dissolution or disappearance.

Melting experiments were used to determine the solidus temperature. The initially crystalline granite powder was used as a starting material, and the solidus temperature is that at which glass first appears in the quenched run product.

3.3. Identification and analysis of the run products

The run products were examined by petrographic microscope, X-ray diffraction, SEM, and electron microprobe. The major phases encountered include crystals (<50 μm, mostly <30 μm) of quartz, alkali feldspars (K-feldspar and albite), mica and topaz, a quenched glass (silicate melt) and an aqueous fluid (vapor). The major crystalline phases and assemblage are almost identical to those in the initial granite sample. Quartz, mica and topaz were easily identified optically, whereas K-feldspar and albite were distinguished based on electron microprobe and X-ray diffraction analysis. Crystal percentages (Table 2) of the run products were estimated by optical microscope, and checked in some cases by point counting of BSE images. These two estimates agree within an error of 5 vol%. Accessory phases such as zircon and fluorite were found in some run products.

The glasses produced in crystallization experiments and crystallization–melting experiments were always colorless with fluid inclusions in homogeneous distribution. No evidence for any quench or equilibrium liquid–liquid immiscibility was found. Crystallization seemed to cease at $T \leq 560$ °C despite the long run durations of up to 30 days, under which approximately 15–25 vol% metastable melt was still present in each run product (with total of crystals 75–85 vol%, Table 2). As demonstrated by Piwinskii and Martin (1970), Pichavant (1987), and London et al. (1989), we believe that the presence of metastable melts at near-solidus is due to slow nucleation and growth of quartz and feldspar from granitic melts. Crystal dissolution rate is thought faster than crystal growth rate (Kuo and Kirkpatrick, 1985), and melting experiments are usually considered to approach equilibrium more rapidly (e.g. Pichavant, 1987; London et al., 1989). The solidus temperature, therefore, was determined using the melting experiments. Glasses produced in the melting experiments were examined under an optical microscope using oil immersion techniques and a gypsum plate, which can detect less than 10 vol% of glass.

The compositions of crystalline phases and quenched glasses were analyzed using the Japan-made JXA-8800 M electron microprobe at Nanjing University. The operation conditions were: acceleration voltage, 15 kV; sample current, 6 nA; counting time on peak, 6 s; beam diameter, 2 μm. The crystalline silicates and topaz were used as analytical standards for major elements and fluorine, respectively, and ZAF correction procedures were used in the analysis. When analyzing the glass composition, the beam was defocused up to a diameter of 20 μm and the counting time was reduced to 2 s to minimize the loss of Na and K during analysis. The data in Tables 1 and 3–6 are averages of multiple analyses (glass: between 2 and 6 spots

Table 2
Experimental results for Xianghualing fluorine-rich leucogranite at 150 MPa (P_{H_2O})

Run no.[a]	Temperature (°C)	Duration (h)	Phases (+vapor)[b]	Ctx[c] (vol%)	LSCT[d] (°C)
C01	800	242	L	–	
C02	780	195	L	–	
C03	760	192	L	–	
CM01	730–760	240–192	L	–	Qz-in 750 ± 10 (liquidus)
CM02	730–750	186–224	L + Qz(diss.)	≪ 1	
CM03	730–740	196–288	L + Qz	1	
C04	740	168	L + Qz	1	
C05	720	192	L + Qz + Afs	3	
CM04	710–730	217–165	L + Qz + Afs(diss.)	<2	Afs-in 730 ± 10
CM05	700–720	233–171	L + Qz + Afs	3	
C06	700	266	L + Qz + Afs	25	
CM06	680–700	178–215	L + Qz + Afs	28	Ms-in 690 ± 10
C07	680	326	L + Qz + Afs + (Mc)	35	
C08	660	267	L + Qz + Afs + (Mc)	42	
C09	640	358	L + Qz + Afs(t) + (Mc)	58	
CM07	630–640	235–278	L + Qz + Afs(t) + (Mc)	55	Afs(t)-in 645 ± 5
CM08	630–650	296–232	L + Qz + Afs + (Mc)	55	
CM09	630–660	246–321	L + Qz + Afs + (Mc)	45	
C10	620	356	L + Qz + Afs(t) + Mc	70	
C11	600	295	L + Qz + Afs(t) + Mc	72	
C12	580	372	L + Qz + Afs(t) + Mc	75	
C13	560	285	L + Qz + Afs(t) + Mc	75	Top-in 550 ± 10
C14	540	721	L + Qz + Afs(t) + Mc + (Top) + (Ft)	80	
C15	520	668	L + Qz + Afs(t) + Mc + Top	75	
M01	500	246	No glass	100	
M02	520	265	No glass	100	
M03	540	368	<15 vol% glass	>85	
M04	520	276	No glass	100	Solidus 530 ± 10
M05	540	286	<20 vol% glass	>80	

[a] Run no.: C01–16, crystallization experiments; CM01–09, crystallization–melting experiments with two-stage durations; M01–05, melting experiments.
[b] Phases (+vapor): Qz = quartz, Afs = alkali feldspar solid solution, Afs (t) = two alkali feldspars (one K-rich, the another Na-rich), Mc = mica, Top = topaz, Ft = fluorite, ( ) = trace-small amount (≪ 1 vol%), diss. = crystals dissolving, L = silicate melt, vapor phase present in all runs.
[c] Ctx (vol%): content of crystalline phases.
[d] LSCT: liquidus, solidus and crystalline phase appearance (-in) temperatures.

each; crystalline phases: between 1 and 5 crystals analyzed per sample). In order to check the quality of the microprobe analysis for glass composition, comparisons were made between microprobe analysis and wet chemical analysis (Table 1). For the dry starting glass, there is excellent agreement between these two analyses within 3% of relative variation for most constituents except for the trace components TiO_2 and P_2O_5. If the deviation of the total from 100% is considered to be an estimate of the H_2O content of the melt and the analyses are normalized to 100%, the microprobe analysis of the superliquidus hydrous glasses is also in good agreement with the wet chemical analysis of dry glass for most constituents, except for Na_2O, K_2O and F with relative errors within <20, <10, and <10%, respectively. The loss of alkali during microprobing leads to a slight increase of the calculated A/NKC and a slight decrease of the Na/K for the hydrous glasses (Table 1). These comparisons, and the fact that two analyses of the superliquidus glasses (C01 and C02 in Table 1) are nearly identical, demonstrate the reliability of our microprobe analysis for the hydrous glasses.

The aqueous vapor phase is present in all runs as indicated by release of a small amount of aqueous solution when opening the capsules, by swollen capsules that hissed when punctured, and by the presence of numerous fluid inclusions trapped in glass. No attempt was made to analyze the vapor phase. The amount of vapor in most runs is very small, and the melt composition in these runs is not considered to be modified significantly by incongruent dissolution. But the quantity of melt in runs near the solidus is small and the quantity of vapor (relative to the melt) is larger than in other runs. The roughly estimated amount of aqueous vapor phase in a run with 80% crystallization accounts for up to 36 wt% of the total residual melt + vapor. Such an aqueous fluid may modify indispensably the composition of residual melt by incongruent dissolution. Trace amounts of low index isotopic solids (~5 μm) were observed on the surface of quenched charges of near-solidus runs. Scaning electron microscopy revealed that these solids consist mainly of Na, K and F, probably the mixture of NaF and KF precipitated from aqueous fluids during quenching. These quenched solids prove that the effect of the vapor

Table 3
Electron microprobe analyses of feldspars (wt%)

Run	C05	CM05	C06	CM06	C08	CM09	CM08	C09	C09	CM07	CM07	C11	C11	C14	C14
T (°C)	720	700, 720	700	680, 700	660	630, 660	630, 650	640	640	630, 640	630, 640	600	600	540	540
N	1	2	4	5	4	3	5	2	2	3	1	3	5	1	3
SiO_2	66.59	66.81	66.38	65.87	65.16	65.18	65.32	66.69	67.13	66.98	67.16	67.15	69.56	70.12	67.02
Al_2O_3	18.06	18.69	18.17	18.23	17.69	17.72	17.81	18.54	19.32	18.43	19.25	18.66	18.73	17.65	17.63
K_2O	11.92	11.89	13.34	13.16	14.86	15.41	14.92	9.42	2.21	9.74	2.42	10.28	1.76	1.65	10.51
Na_2O	2.93	3.14	2.49	2.54	0.91	1.1	0.97	4.87	10.37	4.82	10.08	4.76	10.37	10.86	4.63
CaO	0.36	0.51	0.21	0.16	–	0.01	–	–	–	–	–	–	–	–	–
Total	99.86	101.04	100.59	99.96	98.62	99.42	99.02	99.53	100.03	99.97	98.91	100.85	100.42	100.28	99.79
Si	6.05	6.02	6.04	6.02	6.07	6.04	6.05	6.03	5.98	6.04	5.98	6.02	6.07	6.13	6.08
Al	1.93	1.98	1.94	1.96	1.93	1.94	1.95	1.97	2.02	1.96	2.02	1.97	1.93	1.82	1.88
K	1.38	1.36	1.55	1.54	1.77	1.82	1.77	1.09	0.26	1.13	0.28	1.17	0.20	0.19	1.22
Na	0.51	0.55	0.44	0.46	0.17	0.20	0.18	0.86	1.69	0.84	1.74	0.83	1.75	1.84	0.82
Ca	0.07	0.05	0.02	0.02	–	–	–	–	–	–	–	–	–	–	–
Or	70	69	77	76	91	90	91	56	13	57	14	59	10	9	60
Ab	26	28	22	23	9	10	9	44	87	43	86	41	90	91	40
An	2	3	1	1	–	–	–	–	–	–	–	–	–	–	–

N = number of microprobe analyses; uncertainties are 0.6% (SiO_2), 1.5% (Al_2O_3) and 5% (Na_2O and K_2O); structural formulae are calculated on the basis of 16 O atoms.

Table 4
Electron microprobe analyses of micas (wt%)

Run no	C07	C08	CM09	CM08	C09	C10	C11	C12	C14
T (°C)	680	660	630 660	630 650	640	620	600	580	540
N	1	1	2	1	2	2	3	1	2
SiO_2	38.66	48.11	45.88	43.55	39.35	41.44	39.91	40.34	40.74
Al_2O_3	20.60	20.12	22.60	24.77	21.31	13.82	13.54	12.12	16.61
FeO	26.53	20.51	18.54	17.44	25.84	29.08	30.73	31.40	25.96
MnO	–	0.40	0.38	0.51	0.04	0.13	0.10	0.08	0.10
MgO	0.31	0.42	0.41	0.93	0.34	0.62	0.58	0.56	0.33
K_2O	8.10	7.13	7.84	8.34	8.37	7.73	7.85	7.86	8.48
Na_2O	0.22	0.75	0.52	0.46	0.02	0.29	0.28	0.18	0.20
F	2.48	2.64	2.82	3.97	4.12	4.44	5.59	4.44	5.58
2F=O	−1.05	−1.11	−1.19	−1.67	−1.74	−1.87	−2.36	−1.87	−2.35
Total	95.85	98.97	97.80	98.30	97.65	95.68	96.22	95.11	95.65
Si	6.05	6.98	6.73	6.36	5.99	6.48	6.24	6.43	6.30
Al(IV)	1.95	1.02	1.27	1.64	2.01	1.52	1.76	1.57	1.70
Al(VI)	1.85	2.42	2.64	2.62	1.80	1.03	0.74	0.71	1.33
Fe(VI)	3.12	2.24	2.05	1.92	2.95	3.42	3.62	3.76	3.02
Mn(VI)	–	0.05	0.05	0.06	–	0.02	0.01	0.01	0.01
Mg(VI)	0.07	0.09	0.09	0.20	0.08	0.15	0.12	0.13	0.08
Li(VI)[a]	0.96	1.20	1.17	1.20	1.17	1.38	1.51	1.39	1.56
K	1.62	1.32	1.47	1.55	1.62	1.54	1.57	1.60	1.67
Na	0.07	0.21	0.15	0.13	0.01	0.09	0.09	0.06	0.06
F	1.23	1.21	1.31	1.83	1.98	2.20	2.27	2.23	2.73
OH[b]	2.77	2.79	2.69	2.17	2.02	1.80	1.73	1.77	1.27

N = number of microprobe analyses; uncertainties are 1.2% (SiO_2), 0.5% (Al_2O_3 and FeO), 3% (K_2O and F), 5% (Na_2O, MnO and MgO); structural formulae are calculated on the basis of 24 (O, OH, F) atoms.

[a] Li is assumed present. Li(VI) was estimated by the assumption that the number of cations in the octahedral site of mica is 6, and the Li(VI) = 6 − [Al(VI) + Fe(VI) + Mn(VI) + Mg(VI)].

[b] F is assumed to substitute OH in the mica. OH=4-F.

phase on the modification of melt composition is not negligible in the near-solidus experiments. This effect will be addressed in detail in Section 4.2.

4. Experimental results

Experimental results are given in Table 2. Analytical data for the crystalline phases and coexisting quenched glasses are presented in Tables 3–6.

4.1. Liquidus, solidus, and the characteristics and composition of crystalline phases

The liquidus temperature was determined by crystallization experiments and crystallization–melting experiments to be 750 ± 10 °C, and the solidus temperature was located at 530 ± 10 °C by melting experiments (Table 2). The crystallization/melting interval between liquidus and solidus is 220 °C.

Quartz is the first crystalline phase to appear at the liquidus temperature. It crystallized at 740 °C and did not melt completely at 750 °C in the crystallization–melting experiment (Table 2). However, the morphology of quartz at 750 °C shows a characteristic of resorption, indicating dissolution of quartz. Because the temperature intervals are 20 and 10 °C, respectively, for the crystallization experiments and crystallization–melting experiments, the upper stability temperature of quartz is estimated to be 750 ± 10 °C. Quartz crystals were always distributed homogeneously in the glass as euhedral or subhedral grains with mostly hexagonal bipyramids (β-quartz morphology). At $T < 600$ °C, the prism faces of quartz crystals (α-quartz morphology) were observed. The volume proportion of

Table 5
Electron microprobe analyses of topaz (wt%)

Run no	C14	C15	C16
T (°C)	540	520	500
N	1	1	2
SiO_2	32.03	31.22	32.51
Al_2O_3	57.63	57.65	56.91
F	20.10	19.71	20.20
2F=O	−8.46	−8.30	−8.50
Total	101.30	100.28	101.12
Si	0.97	0.95	0.98
Al	2.05	2.07	2.03
F	1.91	1.90	1.93
OH[a]	0.09	0.10	0.07

N = number of microprobe analyses; uncertainties (C16) are 0.5% ($SiO_2$and Al_2O_3), 0.6% (F); Structural formulae are calculated on the basis of 5 O atoms.

[a] OH=2-F.

Table 6
Electron microprobe analyses of quenched glasses (wt%)

Run	C01	CM02	C05	CM05	C06	CM06	C07	CM08	C10	C11	C12	C13	C14
T (°C)	800	730, 750	720	700, 720	700	680, 700	680	630, 650	620	600	580	560	540
Ctx %	–	≪ 1	3	3	25	28	35	55	70	72	75	75	80
N	5	6	5	4	3	5	4	3	2	3	2	2	3
SiO_2	71.35	70.76	69.86	69.52	68.53	68.74	68.12	67.63	67.15	66.96	66.33	65.84	65.73
Al_2O_3	13.08	13.12	13.23	13.31	13.85	13.94	14.52	15.37	16.26	16.95	16.92	17.21	17.05
FeO	1.52	1.45	1.49	1.53	1.72	1.92	1.73	1.52	1.34	1.16	0.71	0.63	0.55
CaO	0.34	0.35	0.34	0.35	0.46	0.44	0.49	0.55	0.63	0.66	0.59	0.65	0.56
Na_2O	3.08	3.12	3.25	3.28	3.56	3.61	3.83	4.13	4.38	4.57	4.61	4.74	4.82
K_2O	4.37	4.45	4.41	4.39	4.03	4.08	3.85	3.41	3.35	3.22	2.95	2.87	2.78
F	0.91	0.92	0.94	0.95	1.21	1.26	1.31	1.92	2.67	2.82	3.02	3.15	3.03
2F=O	−0.38	−0.38	−0.39	−0.4	−0.51	−0.53	−0.55	−0.81	−1.12	−1.18	−1.27	−1.32	−1.27
Total	94.27	93.79	93.13	92.93	92.85	93.46	93.3	93.72	94.66	95.16	93.86	93.77	93.25
Si/Al	4.64	4.58	4.49	4.44	4.21	4.19	3.99	3.74	3.51	3.36	3.33	3.25	3.28
A/NKC	1.25	1.24	1.23	1.23	1.25	1.25	1.28	1.34	1.36	1.39	1.43	1.42	1.42
Na/K	1.09	1.06	1.12	1.13	1.34	1.34	1.51	1.84	1.98	2.15	2.37	2.50	2.63

N = number of microprobe analyses; uncertainties are 1.8% (SiO_2), 2% (Al_2O_3 for runs with $T > 600$ °C), 6% (Al_2O_3 for runs with $T \leq 600$ °C), 5% (FeO, CaO, K_2O and F), 10% (Na_2O); the concentrations of TiO_2, MnO, MgO and P_2O_5 are, respectively, <0.1 wt% and not listed; Si/Al is the molar ratio of $SiO_2/2^*Al_2O_3$; A/NKC and Na/K, respectively, are the molar ratios of $Al_2O_3/Na_2O + K_2O + CaO$ and Na_2O/K_2O.

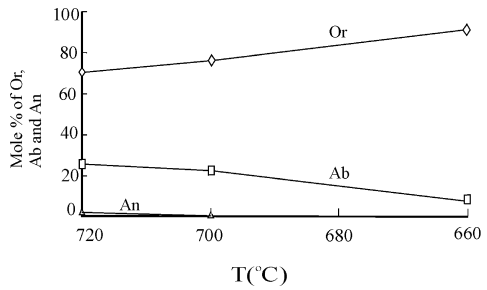

Fig. 2. Compositional variation of alkali feldspars with decreasing run temperature at 150 MPa (P_{H_2O}).

quartz in crystalline phases increased with decreasing temperature.

Alkali feldspar appeared at 720 °C in the crystallization experiments and its complete resorption was observed at 730 °C in the crystallization–melting experiments (Table 2). Thus, the upper stability temperature of alkali feldspar is estimated to be 730 ± 10 °C. Feldspars usually occurred as tabular grains without zoning, twins, patchy intergrowth or graphic structure. The species of feldspar crystals were, therefore, not distinguishable based on their morphologies. Microprobe analysis and X-ray powder patterns show that

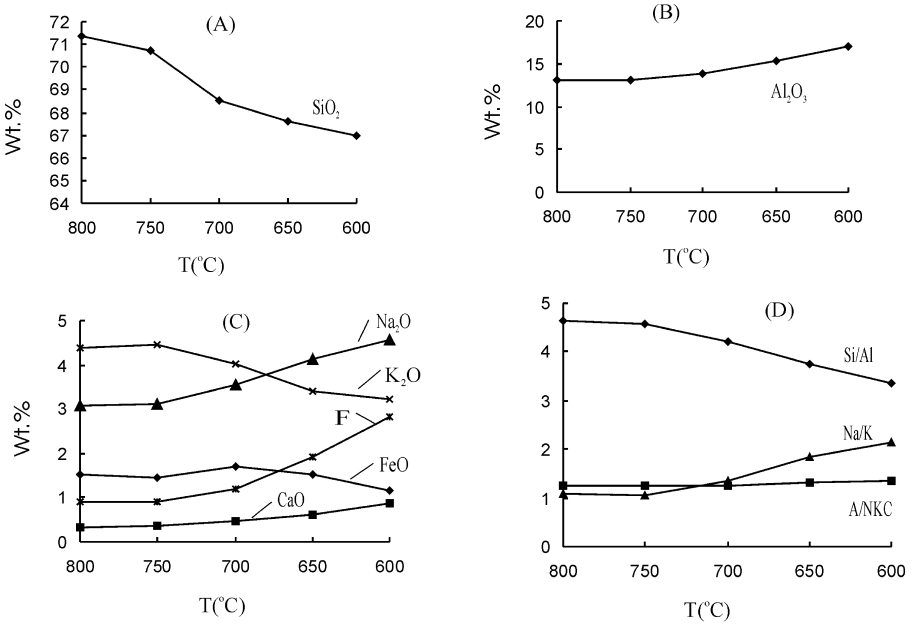

Fig. 3. Compositional variation trend of quenched glasses with decreasing run temperature at 150 MPa (P_{H_2O}). (A) SiO_2 variation trend; (B) Al_2O_3 variation trend; (C) Na_2O, K_2O, CaO, FeO and F variation trends; (D) Si/Al, Na/K and A/NKC variation trends.

all the alkali feldspars forming above 645 ± 5 °C are K-feldspar (K-rich alkali feldspar). Albite (Na-rich alkali feldspar) coexisted with K-feldspar below 645 ± 5 °C (Tables 2 and 3). The structural formulae calculated on the basis of 16 O atoms mostly agree with their stoichiometry, and the anomalously high Si contents in a few analyses (C08, C11 and C14 in Table 3) may result from the partial analysis of the surrounding glass matrix. Above the solvus of alkali feldspar (approximately 645 °C in this experimental system), the Or ($KAlSi_3O_8$) content in alkali feldspars increased and the An ($CaAl_2Si_2O_8$) and Ab ($NaAlSi_3O_8$) contents decreased with decreasing run temperatures (Table 3 and Fig. 2).

Mica appeared at $T = 690 \pm 10$ °C (Table 2) and was usually in the form of hexagonal plates or small flakes. The amount of mica was $\ll 1$ vol% above approximately 600 °C and increased as the temperature decreased. The mica was rich in FeO (total Fe), Al_2O_3 and F, and apparently increased in the content of F with decreasing temperature (Table 4). For the mica in runs with temperatures less than 620 °C, there is an abrupt and notable decrease in Al_2O_3 content and an increase in FeO content, probably indicating disequilibrium for the compositional diffusion in the melts. The structural formulae of mica, calculated on the basis of 24 oxygen atoms, indicate that the number of cations in the octahedral sites is fewer than six. Therefore, we infer that there is Li in the mica, indicating that the species of mica is probably zinnwaldite. The estimated number of Li(VI) increased and OH decreased with decreasing temperature (Table 4).

Topaz appears as euhedral, prismatic or acicular crystals and its upper stability temperature is approximately 20 °C above the solidus temperature of 530 °C (Table 2). The compositions of topaz were homogeneous and constant (Table 5). The structural formulae, calculated on the basis of five oxygen atoms, are close to the stoichiometry of F-topaz (Table 5).

The above results show that quartz is the liquidus crystalline phase and is sequentially followed by K-rich alkali feldspar, zinnwaldite, albite and topaz. The experimental crystallization sequence is consistent approximately with that seen in the corresponding natural sample, implying the experimental conditions may approach the crystallization conditions of the Xianghualing Pluton.

4.2. Composition of quench glass and fractionation trend of residual melt

The chemical compositions of the quenched glasses are presented in Table 6. The H_2O-saturated melts are homogeneous with regard to all measured components up to approximately 75 vol% of crystallization with $T >$ 600 °C as indicated by the small analytical uncertainties in the same run product. The H_2O content of quenched glasses was not directly determined. However, the total of analyzed oxides for the quenched glass suggests the H_2O concentration is between 5 and 7 wt%. This is approximately in the range of H_2O solubility of fluorine-bearing haplogranitic melt measured by Holtz et al. (1993), whose P–H_2O diagram (Fig. 1 in Holtz et al., 1993) shows that the H_2O solubility of haplogranitic melt with <3.11 wt% fluorine ranges from approximately 5.2 to 6.0 wt% at 150 MPa and superliquidus temperature. In consideration of the similar range of fluorine content in the melts (with 0.92–3.15 wt% fluorine, Table 6) and the highly leucogranitic composition for our experimental sample, we believe the H_2O content (solubility) of quenched glasses should be in this range.

The major components of the melt phase are consistent with the starting granite sample, but their contents varied with progressive crystallization and decreasing run temperature. The variation- or fractionation-trends of residual melts are largely independent of the run paths. The residual melts of all crystallization experiments or crystallization–melting experiments evolved to similar compositions at a given final temperature. The most notable fractionation trends in residual melt compositions are the decrease in the SiO_2 and K_2O contents and the Si/Al ratio, and the increase in the contents of Al_2O_3, CaO, Na_2O, F, and the A/NKC and Na/K ratios (Table 6 and Fig. 3) as run temperature decreases. These fractionation trends of residual melt compositions are mainly controlled by the crystallization sequence and the compositions and proportions of the individual crystalline phases in crystalline assemblages. Because F is incompatible in felsic phases and the (K + Na + Ca)/Al ratio in the alkali feldspar is 1:1, fractional crystallization of felsic phases in an initially aluminous F-bearing melt should result in an increase of F content and A/NKC ratio in residual melts. The increasing crystallization of quartz and K-rich alkali feldspar decreases the contents of SiO_2 and K_2O as well as Si/Al ratio, and increases the Na_2O content and Na/K ratio. The content of CaO increased with decreasing run temperature due to the crystallization of Ca-free alkali feldspar at the advanced crystallization stage. Although mica is rich in Al_2O_3 and F, the crystallization of trace-small amounts of mica at relatively high temperature ($\ll 1$ vol% above 600 °C, see Table 2) has little effect on the fractionation trend of Al_2O_3 and F in the residual melts.

Though the sequential crystallization of minerals undoubtedly resulted in the observed fractionation trends of residual melts, the aqueous vapor phase may also exert an influence on the compositional variation of residual melt. The modification of melt composition by the vapor phase may be negligible in most high-temperature runs owing to the relative low extent of crystallization and the low starting fluid/solid ratio. However, the amount of residual melt decreases and the ratio of vapor/residual melt increases with increasing crystallization in the near-solidus runs. The large proportion of aqueous fluid at the late stage of crystallization may have modified the composition of the melt by

incongruent dissolution. Although the solubility of melt components in a vapor phase decreases with decreasing temperature (London et al., 1988), the experiments in the topaz rhyolite–H_2O system (Webster, 1990) revealed that increasing activities of fluorine in magmatic systems increase the solubility of melt components in F-bearing fluid phases. The increase of fluorine in the residual melt at the late stage may therefore increase the partition of fluorine, and accordingly increase the partition of other melt components, into the aqueous fluid (Webster, 1990). The solubility of alkalis in the F-bearing fluid phase is large relative to other melt components. This was proved by the trace amount of Na and K-bearing precipitates on the surface of quenched glass cylinders in the near-solidus experiments. The fluids at the late stage of near-solidus runs may therefore cause an increase in the A/NKC of residual melt and decrease the amount of Na_2O and K_2O. The observed increase in the A/NKC of residual melt in these runs may be caused by the F-bearing fluid phase at the late stage of crystallization in addition to the crystallization of minerals at the early stage.

5. Discussion

5.1. Evaluation of equilibrium

There are three main reaction processes in our experiments: (1) incorporation of H_2O from the aqueous phase into initially dry glass to produce a homogeneous hydrous melt, (2) nucleation and growth of crystals from the hydrous melt (in case of crystallization experiments), and (3) dissolution of crystals (in case of crystallization–melting experiments and melting experiments). In order to discuss the attainment of equilibrium during these experiments, it is important to evaluate the kinetics of each of these three processes.

With a grain size of <50 μm for the starting ground glass, a few tens of minutes are sufficient for H_2O to diffuse throughout ($D_{H_2O} = 3 \times 10^{-8}$ cm^2 s^{-1}, Shaw, 1974). This suggests that production of a homogeneous hydrous melt is rapid. Evidence of a homogeneous distribution of H_2O in the melt is supported by the homogeneous distribution of fluid inclusions (with respect to phase assemblage and volumetric proportions). During the analysis of glasses, significant variations for summation deficiencies were not found, also suggesting a homogeneous distribution of H_2O in the melts.

Crystallization experiments involve nucleation and growth of crystalline phases from the homogeneous hydrous melt. Fenn (1977), Swanson (1977), and Swanson and Fenn (1986) have shown that the nucleation of quartz and feldspar in granitic systems at subliquidus temperatures requires durations ranging from several hours to a few days. In this study, the liquidus and appearance temperatures of quartz, feldspar and mica determined in the crystallization experiments at relatively high temperatures were reversed by crystallization–melting experiments. This is an indication that equilibrium is approached, and that supercooling and nucleation difficulties of these crystalline phases were negligible in these experiments. The generally homogeneous compositions of feldspars, mica and glass (Runs with $T > 600$ °C in Tables 3, 4 and 6) also suggest an approach to phase equilibrium and diffusion equilibrium between melt and crystals. However, for the low-temperature experiments, disequilibrium is obvious. This is indicated by the presence of 15–25 vol% metastable melts in the runs with $T \leq 600$ °C (Table 2), and by the chemical heterogeneity of minerals and melts in these runs. As mentioned in Section 3.3, crystallization seemed to cease at $T = 560$ °C (although the run temperature further decreased), indicating incomplete nucleation and growth of crystals and disequilibrium. The chemical compositions of micas in low-temperature experiments also indicate diffuse disequilibrium in the melts. The Al_2O_3 contents of micas in the runs with $T \leq 620$ °C are obviously low and there is significant variations in Al_2O_3 and FeO contents (Table 4). The residual melt compositions in these runs are very peraluminous, but the micas are relatively Al-depleted, which may indicate that the diffusion of Al in the melt in low-temperature experiments was slow and did not reach equilibrium. The diffuse disequilibrium of Al is also indicated by analytical uncertainties of melt composition in low-temperature experiments. Analytical uncertainty for the Al_2O_3 content in a low-temperature run with $T \leq 600$ °C is always larger than in a high-temperature run (see the note in Table 6).

In the absence of direct experimental information on the rates of crystal dissolution in a granitic melt, it is difficult to evaluate precisely the time required for dissolution equilibrium of crystals in our crystallization–melting experiments and melting experiments. However, most previous authors agree that crystal dissolution is kinetically controlled by diffusion of crystal components in the melt (Donaldson, 1985; Kuo and Kirkpatrick, 1985) and that crystal dissolution rates are faster than crystal growth rates (Kuo and Kirkpatrick, 1985; Piwinskii and Martin, 1970). Considering that (1) the small sizes (<50 μm) of the crystalline phases of run products and the starting granite powder of the melting experiments, and (2) the H_2O saturation in experimental charges which promotes the melting (dissolution) rate, superheating should not occur in our experiments. There is general agreement in the phase assemblages and the compositions of crystals and glasses between crystallization–melting experiments and crystallization experiments with the same run temperature. There is also agreement between melting experiments with the same run temperature but different run durations (Table 2). These general agreements suggest an approach to the equilibrium of crystal

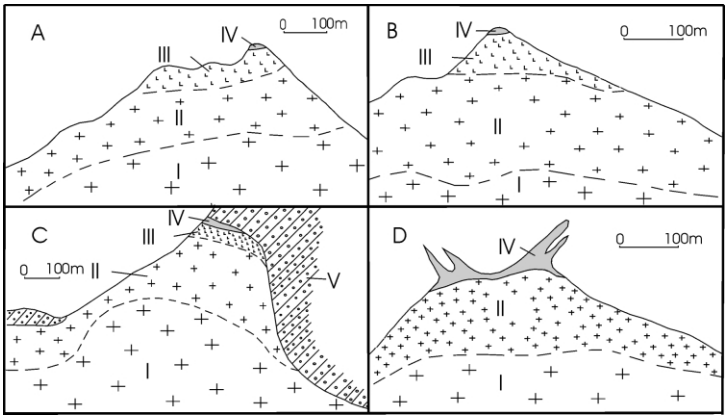

Fig. 4. Examples of vertical zonation of F-rich leucogranite plutons in South China. (A): Xianghualing Pluton, located in South Hunan Province; (B): Xianghuapu Pluton, located in South Hunan Province; (C): Hailuoling Pluton, located in Southeastern Jiangxi Province; (D): Limu Pluton, located in North Guangxi Province;(A, B, and C from Ren et al. (1993); (D) modified after Zhu et al. (2001)). (I): topaz-bearing albite–microcline granite or two mica leucogranite; (II): topaz–albite granite or topaz–Li–mica–albite granite; (III): topaz greisen; (IV): pegmatoid stockscheider; (V): metamorphic sandrock (wallrock).

dissolution in both the crystallization–melting and melting experiments.

From the above discussion, we can conclude that the liquidus and solidus temperatures, the crystallization sequence and the melt-fractionation trends at $T > 600$ °C are reliable. For the low-temperature crystallization-experiments with $T \leq 600$ °C, however, the experimental results need to be treated carefully.

5.2. Crystallization sequence and melt fractionation

The experimental results show that quartz and K-rich alkali feldspar are preferential crystalline phases relative to albite in the F-rich leucogranitic melt; the Or content in alkali feldspar increases and the An and Ab contents decrease with decreasing run temperature. The most obvious fractionation trends of residual melt composition are the decreases in SiO_2 and K_2O contents and Si/Al ratios, and the increases in the contents of Al_2O_3, CaO, Na_2O, and F in addition to A/NKC and Na/K ratios. We believe that these results are mainly caused by the progressive increase in the abundance of fluxing components in the residual melts during crystallization. In the experimental charge, the probable fluxing components include F, H_2O and Li. Considering the H_2O-saturated condition and the low Li_2O content in the starting material, we believe that the increase in fluorine content in the residual melt is the most important factor influencing the experimental results.

As discussed by London et al. (1989) and London (1992) for the H_2O-, B-, P-, and F-rich macusanite system, we believe the observed crystallization sequence and melt fractionation trends stem from selective speciation of the volatile component F (and partly H_2O) with the melt components Si, Al, Ca, Na and K. Spectroscopic studies of F-bearing glasses have shown that F preferentially complexes with Al, Na, and Ca in the melt relative to Si and K (Mysen and Virgo, 1985; Luth, 1988; Kohn et al., 1991; Schaller et al., 1992). Such a behavior for fluorine could increase the activities of SiO_2 and $KAlSi_3O_8$ (Or) and decreases in the activities of $NaAlSi_3O_8$ (Ab) and $CaAl_2Si_2O_8$ (An) in the melt, implying the preferential crystallization of quartz and K-rich alkali feldspar and sodic and silica-poor fractionation trends of the residual melt.

6. Summary and applications

The liquidus and solidus temperatures, crystallization sequence and melt fractionation trends of the F-rich leucogranite from the Xianghualing Pluton have been experimentally determined at 150 MPa (P_{H_2O}). The main results include:

1. The liquidus and solidus temperatures are 750 ± 10 and 530 ± 10 °C, respectively, and the crystallization/melting interval is 220 °C. Quartz is the liquidus phase and is sequentially followed by K-rich alkali feldspar, zinnwaldite, albite and topaz.
2. The Or content in alkali feldspar increases and the Ab and An contents decrease with decreasing temperature. At least in the range of temperature from liquidus to 600 °C, the fractionation trends in residual melt compositions include decreases in the SiO_2 and K_2O content and Si/Al ratio, and increases in the contents of Na_2O, Al_2O_3, CaO, F, and ratios of A/NKC and Na/K.

These experimental results shed light on the crystallization process and vertical zonation of the Xianghualing Pluton and other H_2O-rich, high-level, F-rich leucogranite plutons. This also illustrates the enrichment processes of incompatible elements and ore metals during fractional crystallization of F-rich magma.

6.1. Fractional crystallization and vertical zonation of F-rich leucogranitic pluton

F-rich leucogranites occur extensively in South China and elsewhere, and can generally be shown from field relations to have been emplaced as high-level and late stage plutons of a composite granite body. Vertical zonation usually occurs in such highly evolved granite plutons. From base to top, the following zones can be clearly recognized (see Fig. 4: four examples from South China): (1) topaz-bearing albite–microcline granite zone or topaz-bearing two mica granite zone, (2) topaz–albite granite zone or topaz–Li–mica–albite granite zone, (3) topaz greisen zone, and (4) pegmatoid stockscheider zone. Some Russian geologists suggested that the vertical zones in F-rich plutons were formed by the metasomatism of postmagmatic fluids (Beus et al., 1962; Beus and Zalashkova, 1964).

Much progress has been made regarding the petrogenesis of F-rich granitic rocks in recent years: (1) There usually exist melt inclusions in the quartz and topaz of albite granites and albite–microcline granites (Xia and Chen, 1984; Chang, 1985; Chang and Huang, 1998). (2) The volcanic and subvolcanic analogues of topaz albite granite such as topaz rhyolites (Burt et al., 1982; Congdon and Nash, 1988; Raimbault and Burnol, 1998) and ongonites (Kovalenko, 1973; Huang and Du, 1988; Kortemeier and Burt, 1988; Zhu et al., 1993) are found in many places of the world. (3) Experimental investigations of phase equilibria and physical and chemical properties in F-containing granitic systems demonstrated that granitic magmas rich in fluorine and other volatiles have solidus temperatures of less than 600 °C (Manning, 1981; Webster et al., 1987; London et al., 1989; Xiong et al., 1999), and low viscosity and density (Dingwell, 1985; Dingwell et al., 1993). These results increasingly suggest that magmatic crystallization may be the major process at least for the formation of topaz-bearing albite granite and albite–microcline granite (Zhu et al., 1993, 2001; Pollard, 1995; Xiong et al., 1999), although there remain disputes as to the origin (magmatic or hydrothermal) of topaz greisens and pegmatoid stockscheiders in the apical zones (Hu and Sun, 1984; Zhu et al., 1993). The experimental data presented in this paper provide new insights into the evolution and development of zonation in F-rich granite plutons. The low solidus temperature and large crystallization/melting temperature interval suggest that F-rich granitic magma has a prolonged crystallization history. The preferential crystallization of quartz and K-rich alkali feldspar causes sodic and silica-poor differentiation trends in the residual melt. The extreme increase of fluorine content at the advanced crystallization stage results in strong depolymerization and decrease in viscosity and density of the residual melt, and accelerates crystal fractionation and chemical and mineralogical zonation of the F-rich granitic plutons. The experimental results also have important applications for understanding the derivation of ongonite and topaz rhyolite melts, which are compositionally analogous to topaz albite granites. Such F-rich, sodic residual melts were probably formed at depth by fractional crystallization of initially potassic granitic magmas, which then ascended and were injected into surrounding rocks to crystallize as ongonite dykes, or erupted onto surface as topaz rhyolite magmas.

6.2. Enrichments of incompatible elements and ore metals

F-rich leucogranitic rocks usually contain elevated concentrations of incompatible elements and ore metals, such as Li, Be, Rb, Cs, W, Sn, Nb, Ta, U, and Th. Some of them can be enriched to economic concentrations in the apical part of a pluton. Magmatic differentiation may have a significant effect on the enrichment of these elements.

Biotite and accessory phases, such as zircon, monazite, sphene, and rutile, are the major carriers of incompatible elements and ore metals in many granitic rocks. They may cause enrichment or depletion of trace elements in residual melts during fractional crystallization. Ore metals may be removed from melts by the precipitation of accessory phases and by substitution into biotite, thus reducing the potential for incompatible element mineralization. However, F-rich granitic rocks are usually highly leucogranitic. Biotite in such granitic rocks is rarely abundant, and usually occurs at the late crystallization stage, as in the case of the Xianghualing granite, Pleasant Ridge zinnwaldite–topaz granite (Taylor, 1992) and Cornwall granite (Weidner and Martin, 1987). It may not significantly change the differentiation behavior of trace elements in F-rich leucogranitic systems. Our experimental data also prove that the mica in F-rich leucogranite systems is not a preferential crystallization phase. The preferential crystallization of felsic phases in F-rich leucogranitic systems will cause an apparent increase in incompatible components, such as volatiles and trace elements, in the residual melt. In addition, the progressive enrichment of fluorine during crystallization will significantly decrease the activity coefficients of trace elements in granitic melts via formation of F-complexes or changing melt structure. Such an effect may drastically increase the solubility of accessory phases and decrease the biotite/melt and accessory phase/melt partition coefficients of trace elements, and may therefore result in the enrichment of ore metals in residual melts. Some experimental studies (Keppler, 1993; Linnen, 1998) have demonstrated that fluorine may significantly increase the solubility of accessory phases in granitic melts. More experimental investigations are necessary to understand the effects of fluorine on trace-element partitioning behavior of biotite/melt and accessory phase/melt in granitic systems.

Acknowledgments

We would like to thank Mr Ming-Yuan Lai who assisted during the electron microprobe analysis. Deep appreciation also goes to K. Burke, J.D. Webster and D.M. Burt for their valuable comments, helpful suggestions and corrections in English. This work is supported by the Major State Basic Research Program of People's Republic of China (G1999043202), the National Nature Science Foundation of China (49973022 and 49873017), Chinese Academy of Sciences (KZCX2-102 and KZCX2-SW-117) and Visiting Scholar Foundation of Key Laboratory in University of China.

References

Bailey, J.C., 1977. Fluorine in granitic rocks and melts: a review. Chemical Geology 19, 1–42.

Beus, A.A., Zalashkova, N.Y., 1964. Postmagmatic high-temperature metasomatic processes in granitic rocks. International Geology Review 6, 668–681.

Beus, A.A., Severov, E.A., Sitinin, A.A., Subbotin, R.D., 1962. Albitized and Greisenized Granites (Apogranites), Moscow Academic Science Press, Moscow, pp. 194, in Russian.

Burt, D.M., Sheridan, M.F., Bikun, J.V., Christiansen, E.H., 1982. Topaz rhyolites—distribution, origin and significance for exploration. Economic Geology 77, 1818–1836.

Chang, H.L., 1985. A study on melt inclusions in the topaz phenocrystals of Xianghualing aplite dyke, Hunan Province. Bulletin of Yichang Institute for Geology and Mineral Resources, Chinese Academy of Geological Sciences 9, 33–41, in Chinese.

Chang, H.L., Huang, H.L., 1998. Melt-fluid inclusions in topaz from the Xianghualing topaz granite in Linwu County, Hunan Province. Acta Petrologica et Mineralogica 17 (1), 81–87, in Chinese with English abstract.

Congdon, R.D., Nash, W.P., 1988. High-fluorine rhyolites: an eruptive pegmatite magma at the Honeycomb Hills Utah. Geology 16, 1018–1021.

Dingwell, D.G., 1985. The structure and properties of fluorine-rich magmas: a review of experimental studies. In: Taylor, R.P., Strong, D.F. (Eds.), Recent Advances in the Geology of Granite-Related Mineral Deposits, Canadian Institute of Mining and Metallurgy, pp. 1–12.

Dingwell, D.G., Scarfe, C.M., Cronin, D.J., 1985. The effect of fluorine on viscosity in the system Na_2O–Al_2O_3–SiO_2: implications for phonolites, trachytes, and rhyolites. American Mineralogist 70, 80–87.

Dingwell, D.G., Knoche, R., Webb, S.L., 1993. The effect of F on the density of haplogranite melt. American Mineralogist 78, 325–330.

Donaldson, C.H., 1985. The rates of dissolution of olivine, plagioclase, and quartz in a basalt melt. Mineralogical Magazine 49, 683–693.

Fenn, P.M., 1977. The nucleation and growth of alkali feldspars from hydrous melts. Canada Mineralogist 15, 135–161.

Holtz, F., Dingwell, D.B., Behrens, H., 1993. Effects of F, B_2O_3 and P_2O_5 on the solubility of water in haplogranite melts compared to natural silicate melts. Contributions to Mineralogy and Petrology 113, 492–501.

Hu, S.X., Sun, M.Z., 1984. An important metallogenetic model for W, Sn, and rare granitophile element ore deposits related to metasomatically altered granites. In: Xu, K.Q., (Ed.), Geology of Granites and their Metallogenetic Relations. Jiangsu Press, Nanjing, pp. 519–537.

Huang, Y.H., Du, S.H., 1988. Rocks, Mineral Deposits and Minerals in Xianghualing District, Science and Technology Press, Beijing, in Chinese with English abstract.

Keppler, H., 1993. Influence of fluorine on the enrichment of high-field-strength trace elements in granitic rocks. Contributions to Mineralogy and Petrology 114, 479–488.

Kohn, S.C., Dupree, R., Mortuza, M.G., Henderson, C.M.B., 1991. NMR evidence for five- and six-coordinated aluminum fluoride complexes I F-bearing aluminosilicate glasses. American Mineralogist 76, 309–312.

Kortemeier, W.T., Burt, D.M., 1988. Ongonite and topazite dikes in the Flying Ranch area, Tonto basin, Arizona. American Mineralogist 73, 507–523.

Koster van Groos, A.F., Wyllie, P.J., 1968. Melting relationships in the system $NaAlSi_3O_8$–NaF–H_2O to 4 kbars pressure. Journal of Geology 76, 50–70.

Kovalenko, V.I., 1973. Distribution of fluorine in a topaz bearing quartz keratophyre (ongonite) and the solubility of fluorine in granitic melts. Geochemical International 10, 41–49.

Kovalenko, V.I., 1978. The reactions between granite and aqueous hydrofluoric acid in relation to the origin of fluorine-bearing granites. Geochemical International 14, 108–118.

Kuo, L.C., Kirkpatrick, R.J., 1985. Kinetics of crystal dissolution in the system diopside–forsterite–silica. American Journal of Science 285, 51–90.

Linnen, R.B., 1998. The solubility of Nb–Ta–Zr–Hf–W in granitic melts with Li and Li + F: constraints for mineralization in rare metal granites and pegmatites. Economic Geology 93, 1013–1025.

Liu, C.S., Ling, H.F., Xiong, X.L., Shen, W.Z., Wang, D.Z., Huang, X.L., Wang, R.C., 1999. An F-rich, Sn-bearing volcanic-intrusive complex in Yanbei, South China. Economic Geology 94, 325–342.

London, D., 1992. The application of experimental petrology to the genesis and crystallization of granitic pegmatites. Canada Mineralogist 30, 499–540.

London, D., Hervig, R.L., Morgan, G.B., 1988. Melt-vapor solubilities and elemental partitioning in peraluminous granite–pegmatite systems: experimental results with Macusani glass at 200 MPa. Contributions to Mineralogy and Petrology 99, 360–373.

London, D., Morgan, G.B., Hervig, R.L., 1989. Vapor-undersaturated experiments with Macusani glass +H_2O at 200 MPa and the internal differentiation of granitic pegmatites. Contributions to Mineralogy and Petrology 102, 1–17.

Luth, R.W., 1988. Raman spectroscopic study of the solubility mechanisms of F in glasses in the system CaO–CaF_2–SiO_2. American Mineralogist 73, 297–305.

Manning, D.A.C., 1981. The effect of fluorine on liquidus phase relationships in the system Oz–Ab–Or with excess water at 1 kb. Contributions to Mineralogy and Petrology 76, 206–215.

Mysen, B.O., Virgo, D., 1985. Structure and properties of fluorine-bearing aluminosilicate melts: the system Na_2O–Al_2O_3–SiO_2–F at 1 atm. Contributions to Mineralogy and Petrology 91, 205–220.

Pichavant, M., 1987. Effects of B and H_2O on liquidus phase relations in the haplogranite system at 1 kbar. American Mineralogist 72, 1056–1070.

Pichavant, M., Manning, D.A.C., 1984. Petrogenesis of tourmaline granites and topaz granites; the contribution of experimental data. Physics of the Earth and Planetary Interiors 35, 31–50.

Piwinskii, A.J., Martin, R.F., 1970. An experimental study of equilibrium with granitic rocks at 10 kbars. Contributions to Mineralogy and Petrology 29, 1–10.

Pollard, P.J., 1995. Geology of rare metal deposits: an introduction and overview. Economic Geology 90, 489–494.

Raimbault, L., Burnol, L., 1998. The Richemont Rhyolite Dyke, Massif Central, France: a subvolcanic equivalent of rare-metal granites. Canada Mineralogist 36, 265–282.

Ren, Q.J., Hu, Z.H., Yan, Z.F., 1993. Mineral Deposits, Press of Nanjing University, Nanjing, pp. 77, in Chinese.

Schaller, T., Dingwell, D.B., Keppler, H., Knoller, W., Merwin, L., Sebald,

A., 1992. Fluorine in silicate glasses: a multinuclear magnetic resonance study. Geochimica et Cosmochimica Acta 56, 701–707.

Shaw, H.R., 1974. Diffusion of H_2O in granitic liquid, I—experimental data, II—mass transfer in magma chambers. In: Hofmann, A.W., Giletti, B.J., Yoder, H.S. Jr., Yund, R.A. (Eds.), Geochemical Transport and Kinetics, vol. 634. Carnegie Institution of Washington, pp. 139–170, Washington Publication.

Swanson, S.E., 1977. Relation of nucleation and crystal-growth rate to the development of granitic textures. American Mineralogist 66, 966–978.

Swanson, S.E., Fenn, P.M., 1986. Quartz crystallization in igneous rocks. American Mineralogist 71, 331–342.

Taylor, R.P., 1992. Petrological and geochemical characteristics of the Pleasant Ridge zinnwaldite–topaz granite, southern New Brunswick, and comparisons with other topaz-bearing felsic rocks. Canada Mineralogist 30, 895–921.

Webster, J.D., 1990. Partitioning of F between H_2O and CO_2 fluids and topaz rhyolite melt: implications for mineralizing magmatic-hydrothermal fluids in F-rich granitic systems. Contributions to Mineralogy and Petrology 104, 424–438.

Webster, J.D., Duffield, W.A., 1991. Volatiles and lithophile elements in Taylor Creek Rhyolite: constraints from glass inclusion analysis. American Mineralogist 76, 1628–1645.

Webster, J.D., Holloway, J.R., Hervig, R.L., 1987. Phase equilibria of a Be, U and F-enriched vitrophyre from Spor Mountain, Utah. Geochimica et Cosmochimica Acta 51, 389–402.

Webster, J.D., Burt, D.M., Aguillon, R.A., 1996. Volatiles and lithophile trace-element geochemistry of Mexico tin rhyolite magmas deduced from melt inclusions. Geochimica et Cosmochimica Acta 60, 3267–3283.

Weidner, J.R., Martin, R.F., 1987. Phase equilibria of a fluorine-rich leucogranite from the St. Austell pluton, Cornwall. Geochimica et Cosmochimica Acta 51, 1591–1597.

Wyllie, P.J., Tuttle, O.F., 1961. Experimental investigation of silicate systems containing two volatile components. Part II: the effects of NH_3 and HF in addition to water on the melting temperatures of granite and albite. American Journal of Science 259, 128–143.

Xia, W.H., Chen, Z.Y., 1984. The melt inclusions in topaz and quartz and their application on the genesis of Ta, Nb granite in South China. Earth Science 2, 76–83, in Chinese with English abstract.

Xiong, X.L., Zhao, Z.H., Zhu, J.C., Rao, B., 1999. Phase relations in albite granite–H_2O–HF system and their petrogenetic applications. Geochemical Journal 33, 199–214.

Zhu, J.C., Liu, W.X., Zhou, F.Y., 1993. Ongonite and topazite in dyke No.431 of Xianghualing district and their spatial zonation and genetic relationship. Acta Petrologica Sinica 9 (2), 158–166, in Chinese with English abstract.

Zhu, J.C., Li, R.K., Li, F.C., Xiong, X.L., Zhou, F.Y., Huang, X.R., 2001. Topaz–albite granites and rare-metal mineralization in the Limu district, Guangxi Province, southeast China. Mineralium Deposita 36, 393–405.